CHAPTER II

Strontium hexaferrite-LLDPE composite for design of single layer absorber

Content:

2.1 Introduction

Impedance matching at the air-absorber interface and attenuation within the absorber are the primary requirement for a good absorber. The challenge for the designer is to minimise thickness even while meeting these requirements for different applications including the aeronautics industry, radio astronomy and satellite communications.

M-type strontium hexagonal ferrite ($SrFe_{12}O_{19}$) has higher anisotropy (anisotropy constant of 3.5×10^6 erg cm^{-3}) as compared to M-type barium hexagonal ferrite (3.3×10^6 erg cm^{-3}), high saturation magnetization (74.3-92.6 emu/g), low density and high chemical stability [1, 2]. Due to the resonance absorption of moving magnetic domains and spin relaxation at high-frequency electromagnetic field, $SrFe_{12}O_{19}$ has higher losses [3-5] which enhances the wave-attenuation. Strontium hexa-ferrite is a good candidate for developing absorbers. Reduced particle size splits the electronic energy level spacing which lies in the microwave range [6]. These discrete levels attenuate the impinging *em* wave more rapidly as electrons absorb the energy when they move from one level to another. Hence, nanosized strontium ferrite is selected as magnetic filler in the present investigation.

LLDPE is a co-polymer of ethylene and α-olefin. It has a long linear chain and homogeneous short side chain branching. Its linearity provides strength, while the branching provides toughness. The short branches disrupt the uniformity of the

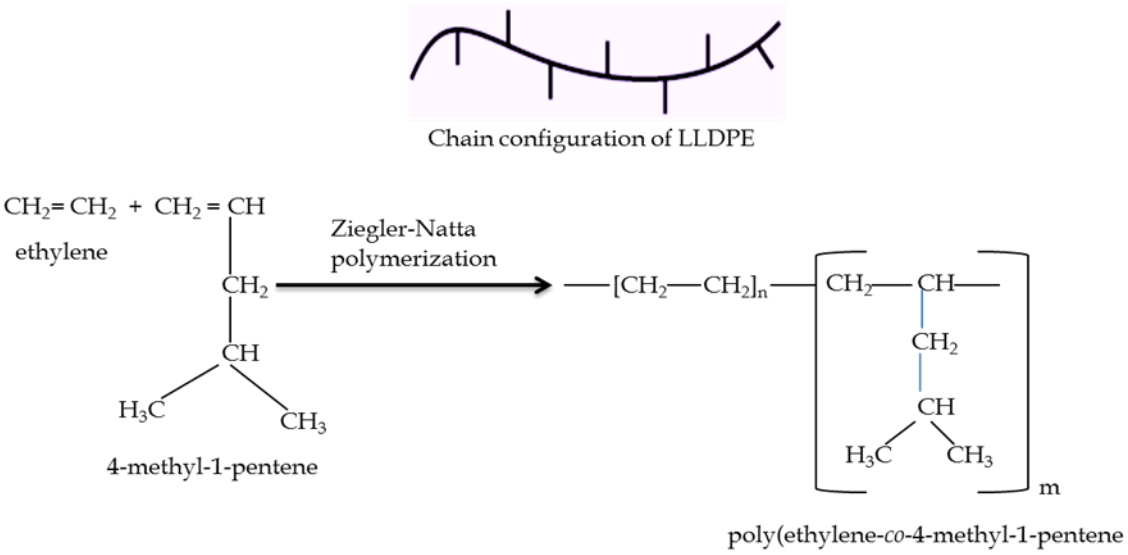

Figure 2.1 Chemical structure of linear low density polyethylene

polymer chain to prevent crystalline formation and achieving high density [9-13]. Figure 2.1 shows the chemical structure of LLDPE using 4-methyl-1-pentene co-monomer. Short side chain branching of LLDPE allows addition of higher percentage of fillers without making the composite brittle. It also has high tensile strength (18.8 MPa), low density (0.915 g/cm^3) and can be moulded easily into thin sheets. LLDPE is an inexpensive polymer with good resistance to chemicals [7-10] and is chosen as matrix to develop composite microwave shields.

The detailed process of synthesis of nanosized filler and fabrication of the composites is presented in this chapter. Comprehensive microstructural studies of the synthesized nanoparticles and nanocomposites are given. Complex permittivity and permeability at microwave frequencies of the composite is measured using the Nicolson-Ross method [11]. Other relevant characteristics for absorbers like saturation magnetization, water absorbance and density are also investigated.

A single layer absorber is designed using the transmission line model (TL model). The thickness of the single layer absorber is optimized so as to achieve better impedance matching to obtain better absorption. Reflection loss of the fabricated single layer absorber is measured in the X-band.

2.2 Synthesis and characterizations

Nanosized strontium ferrite is synthesized using the co-precipitation technique. The comprehensive microstructural details of the synthesized nanoparticles and nanocomposites as well as the results analysis are given. XRD and TEM analysis is carried out to determine the crystalline and particle size. Composites with different wt. % of filler in LLDPE matrix are fabricated and homogeneity of distributions is ascertained from SEM images.

2.2.1 Material synthesis and composite preparation

Nanosized strontium ferrite is synthesized using the co-precipitation technique for its use as magnetic filler. Strontium nitrate (≥ 98% purity, Merck) and iron (III) nitrate nonahydrate (≥ 98% purity, Merck) precursors are used as the base materials to prepare M-type strontium ferrite ($SrFe_{12}O_{19}$) particles. The molar ratio of strontium nitrate to ferric nitrate is taken as 1:12. NaOH is added dropwise to control the size of the particles. Oleic acid is used as surfactant in order to reduce inter-particle interaction and prevent agglomeration. Aqueous solutions of

strontium and iron salts are prepared separately by dissolving the salts in stoichiometric proportion in deionized water (0.1 M in 100 ml). The precipitate formed is then washed with a mixture of distilled water and ethanol to remove the sodium and nitrate compounds followed by drying to remove moisture. The dried powder is then annealed at a constant temperature for 2 hours. Samples are prepared at three different annealing temperatures, 650˚C, 750˚C and 850˚C to obtain three different samples of strontium ferrite powder.

LLDPE powder is sieved to obtain powder with particle size of ≤ 5 μm. Composite specimens of different wt. % are prepared by mechanically blending this sieved LLDPE powder with $SrFe_{12}O_{19}$ (SrM) powder for about an hour. The mixture is then put into the die-mould and cured for 2 hours by heating up to 110˚C. Care is taken to keep the thickness uniform while moulding the sample into a rectangular shape by using fixed spacer in a three piece die mould at a uniform pressure of 36.5 MPa. The sample is then allowed to cool at room temperature. The thickness of the sample is measured using, a digital Vernier calliper (Digimatic Caliper; CD-12”PSX, Mitutoyo Corp., Japan) with a least count of 0.01mm. Thickness of the sample at four different positions are measured with three sets at each position and then the averaged, to minimize errors in measurement, if any.

XRD studies of LLDPE and the strontium ferrite prepared at three annealing temperatures are carried out to determine the crystalline size of samples. FTIR spectroscopy studies of LLDPE, $SrFe_{12}O_{19}$ and $SrFe_{12}O_{19}$-LLDPE composites are conducted to obtain information on the bond structure and interactions among the various constituents in the composites. TEM characterizations of the ferrite and SEM characterization of the synthesized composite are also carried out.

2.2.2 Microstructural characterizations

X-ray diffraction (XRD) studies

XRD patterns (Rigaku, Miniflex 200 X-ray diffractometer) of the matrix and synthesized filler material are obtained using monochromatic Cu Kα radiation (wavelength, λ=1.541841 Å) at room temperature over a 2θ angle from 20˚ to 70˚. The diffraction peaks at 2θ = 21.80˚ and 24˚, corresponds to (110) and (200) diffraction planes of LLDPE respectively [7, 12] which is shown in figure 2.2.

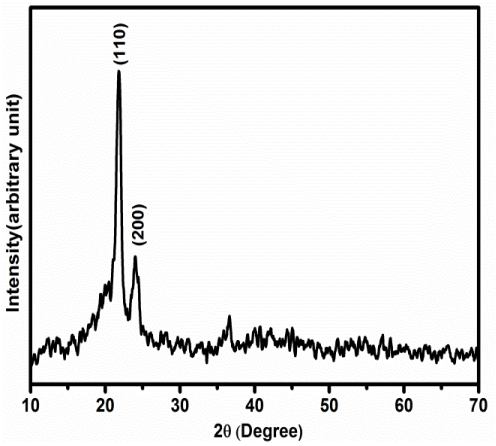

Figure 2.2: XRD pattern of LLDPE

Diffraction pattern of strontium ferrite samples annealed at 650˚C, 750˚C and 850˚C is shown in figure 2.3. The value of lattice parameters are computed using d-spacing value and respective (*h k l*) parameters. Inter-planar distance, *d* is given by

$$\frac{1}{d^2} = \frac{4}{3}\left(\frac{h^2+k^2+l^2}{a^2}\right) + \frac{l^2}{c^2} \tag{2.1}$$

From the most prominent peaks, the average crystalline size (D) is calculated using Debye-Scherrer's equation

$$D = \frac{k'\lambda}{\beta\, cos\theta} \tag{2.2}$$

where, k' is Scherrer's constant, β is full width at half maximum (FWHM) of the particular peak. *The diffraction peaks at* 2θ values of 23.15˚, 29.06˚, 30.34˚, 32.31˚, 34.15˚, 35.17˚, 35.40˚, 39.06˚, 41.17˚, 42.08˚, 44.93˚, 46.85˚, 50.24˚, 53.91˚, 57.18˚, 58.90˚, 60.08˚, 64.81˚, 63.2˚, 64.81˚, 68.16˚ and 69.60˚ corresponds to the strongest diffraction planes (0 0 6), (1 0 6), (1 1 0), (1 0 7), (1 1 4), (2 0 0), (2 0 1), (0 0 10), (2 0 5), (2 0 6), (2 0 7), (1 0 11), (1 1 10), (3 0 0), (2 1 7), (2 0 11), (1 0 14), (2 1 9), (2 2 0), (3 0 0), (2 0 14) and (2 0 8) from the matches in JCPDS # 33-1340, indicating formation of $SrFe_{12}O_{19}$. The lattice constants, a = 5.887 Å and c = 23.047 Å determined from equation (2.1), correspond to hexagonal M-type phase. The average crystalline size calculated from equation (2.2) is given in table 2.1.

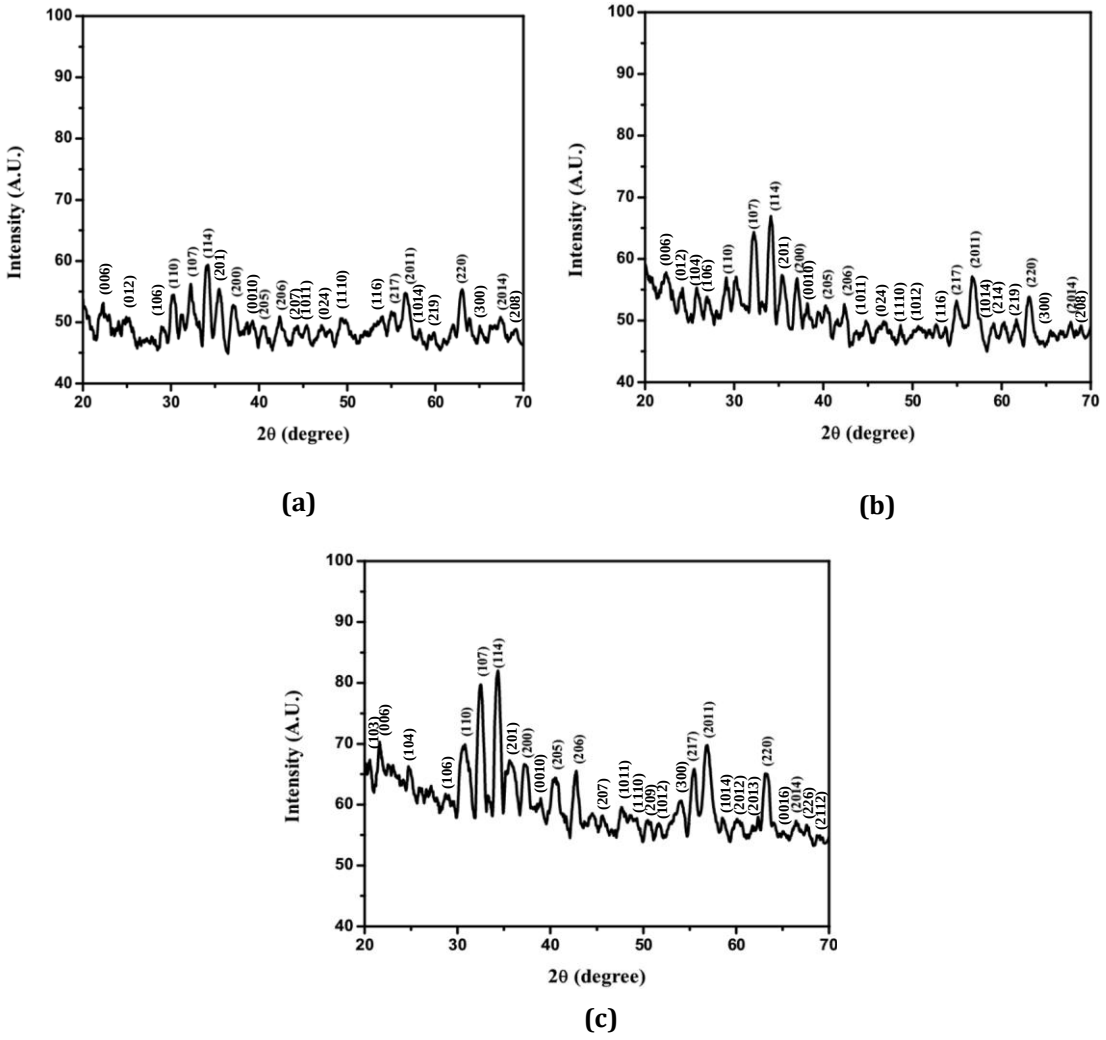

Figure 2.3: XRD pattern of $SrFe_{12}O_{19}$ annealed at **(a)** 650˚C, **(b)** 750˚C and **(c)** 850˚C

The crystalline size of strontium ferrite is in the nanometer range. The grain size of ferrite is observed to increase with increase in annealing temperature, a trait similar to that reported in [13, 14]. At the two lower sintering temperatures studied, i.e., 650˚C and 750˚C, additional diffraction peaks are observed at 26.14˚, 43.52˚, 49.48˚ and 53.7˚ corresponding to the planes (0 1 2), (2 0 2), (0 2 4) and (1 1 6) which is indexed to Fe $(NO_3)_3.9H_2O$ (JCPDS # 39-1346), showing presence of traces of precursors. It is noteworthy that these peaks are absent at 850˚C, as better crystalline structure is formed at higher temperature [13].

Table 2.1: Calculated crystalline size (D) and lattice parameter of $SrFe_{12}O_{19}$

Ferrite	Annealing temperatures	Average crystalline size, D (nm)	Lattice parameters (Å)	
			a	c
$SrFe_{12}O_{19}$	650˚C	16.69	5.861	23.01
	750˚C	24.27	5.875	23.03
	850˚C	25.8	5.887	23.04

Composite samples with different wt. % of nanosized $SrFe_{12}O_{19}$ in LLDPE matrix is developed using strontium ferrite annealed at 850˚C, hereafter referred to as $SrFe_{12}O_{19}$-LLDPE nanocomposite.

Fourier-transform infrared spectroscopy (FTIR)

Fourier transform infrared spectra (FTIR; IMPACT 410, NICOLET, USA) of the samples are obtained in a range between 400 cm^{-1} and 4000 cm^{-1}.

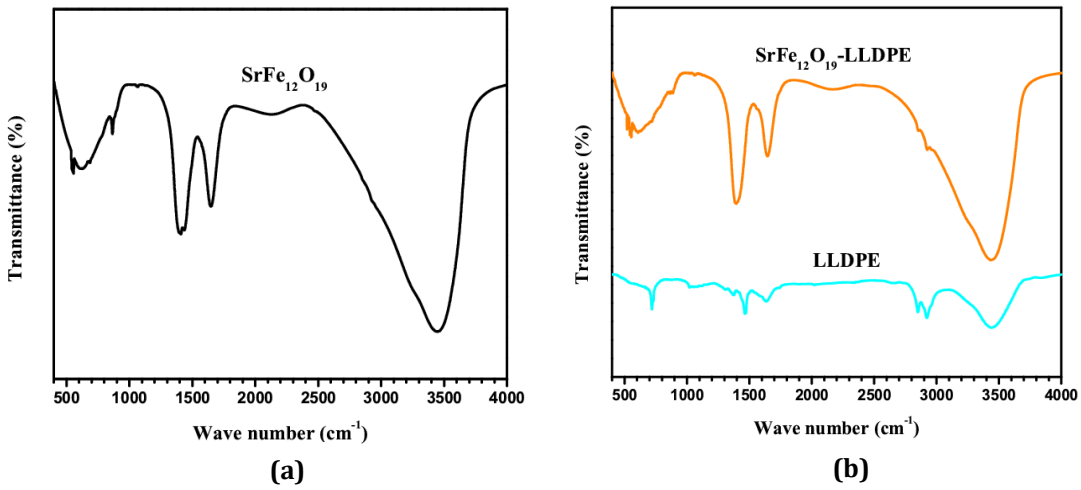

Figure 2.4: FTIR spectra **(a)** $SrFe_{12}O_{19}$ **(b)** LLDPE and $SrFe_{12}O_{19}$-LLDPE composite

The spectra (Figure 2.4) indicates the characteristic bands of the O–H stretching vibration of water at about 1500^{-1} and 3400 cm^{-1}. The powder annealed at 850 ˚C reveals absorption bands at 550 cm^{-1} and 590 cm^{-1}, which are identified as the metal–oxygen stretching vibrations of SrM hexaferrite [15]. The IR spectrum of LLDPE shows two sharp peaks at 2843 cm^{-1} and 2909 cm^{-1} that correspond to the C-H symmetric and asymmetric stretching. CH_2 stretching is seen at 1463 cm^{-1}. The hydroxyl group at 3460 cm^{-1} is the broad peak of the hydrogen bonding in the region 3460 cm^{-1} to 3626 cm^{-1} [16]. The spectrum of the composite shows the presence of both phases of fillers and the matrix and no new peaks has been observed showing that the interaction between $SrFe_{12}O_{19}$ and LLDPE is physical in nature.

Transmission electron microscopy (TEM)

TECNAI G2 20 S-TWIN transmission electron microscope (TEM; FEI Company, USA) operating at an accelerating voltage of 200 kV is used to carry out TEM analysis. The TEM images of $SrFe_{12}O_{19}$ in figure 2.5 (c) confirms elongated hexagonal rod like structure with an observed length of ~78 nm.

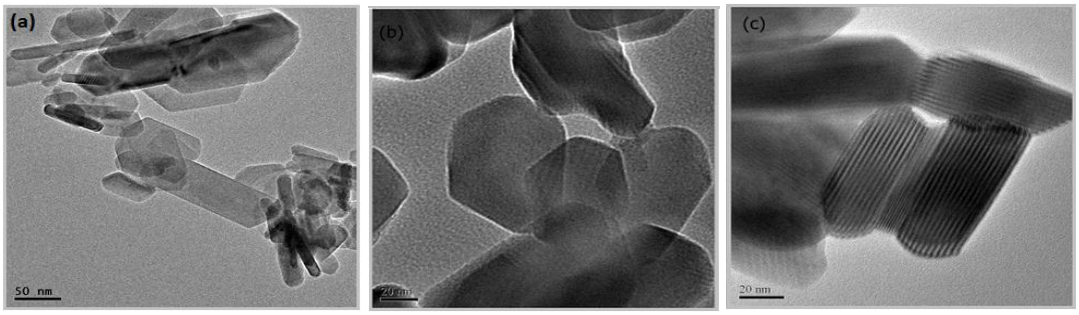

(a) **(b)** **(c)**

Figure 2.5: TEM images of $SrFe_{12}O_{19}$ at (a) 650°C (50nm) (b) 750°C (20nm) (c) 850°C (20nm)

Extended rod like shape in one direction is observed for the particles annealed at 850°C with crystal lattice plane anisotropy. Particle size distributions were estimated by counting about 200 strontium ferrite nanocrystals sintered at 850°C, using ImajeJ software and characterized by a log-normal function. The average particle size is about 78 nm. The surface energy of strontium ferrite is different along different directions of the unit cell. The growth of the nanoparticles along [0001] direction is preferential i.e. the c-axis, as it is energetically favorable due to minimum surface energy at higher temperature and hence, the elongated rod shaped nanostructure formation is observed [17, 18].

Scanning electron microscope (SEM)

Scanning electron micrographs (SEM; JSM 6390LV, JEOL, Japan) are taken at 10^{-11} A probe current and 20 kV accelerating voltage at different resolutions.

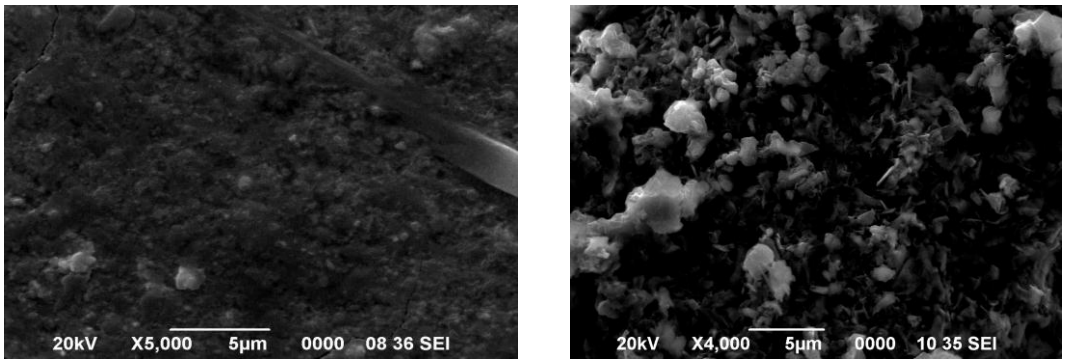

(a) **(b)**

Figure 2.6: SEM images of 60 wt. % of $SrFe_{12}O_{19}$-LLDPE composite

Figure 2.6 shows the SEM micrographs of 60 wt. % $SrFe_{12}O_{19}$-LLDPE nano-composite at different magnification. It is seen that there is no agglomeration

of the filler particles in the matrix and the distribution is uniform in general, thus assuring uniform propagation of *em* wave.

2.2.3 Physical, thermal and magnetic characterizations

Density and Water absorbance

Density measurement of the $SrFe_{12}O_{19}$-LLDPE nano-composite samples are carried out using Archimedes' principle [19]. If weight of the substrate measured in air is W_{air} and W_{app} is the apparent immersed weight when suspended in water, then the experimental bulk density (d_s) of the LLDPE substrate is found as follows

$$d_s = \frac{W_{air}}{W_{air} - W_{app}} \times D_{water} \tag{2.3}$$

where, D_{water} is density of water at room temperature (= 0.997 g/cc at 25˚C)

High moisture or humidity conditions can alter the material properties which can affect the absorber performance. The sample is tested for water absorbance by soaking in water for 72 hours at room temperature. Thereafter the samples are pat-dried. The weight of the sample is measured before and after soaking and % of water absorbed is calculated. The percentage of water absorption is determined from the following expression

$$Water\ absorbance\ (\%) = \frac{W_t - W_0}{W_0} \times 100 \tag{2.4}$$

where, W_t and W_0 are the weights of the material, after and before soaking in water respectively.

Table 2.2 shows the density and water absorbance of 10 to 70 wt. % of $SrFe_{12}O_{19}$-LLDPE nano-composites. There is marginal increase in density of the nano-composite with increase in the ferrite content. The composite shows negligible water absorption. The nominal increase in water absorbance could be due to increase in porosity of the samples with increasing filler concentration.

Thermo Gravimetric Analysis (TGA)

The thermo gravimetric analysis (TGA) is performed to predict the thermal stability of a material in the temperature range of 50˚C to 700˚C. The TGA for $SrFe_{12}O_{19}$-LLDPE composites is carried out in the air atmosphere using Thermal Analyzer (TGA-50, SHIMADZU) and is shown in figure 2.7.

From the curves, it can be seen that the decomposition temperature (onset of inflection) of the composite is around 400˚C with weight loss of 5%. The major weight loss occurs due to growth of volatiles in between the temperature 410-700˚C. Thus, TGA curve shows that the developed composite is stable almost upto 400˚C before they undergo thermal degradation.

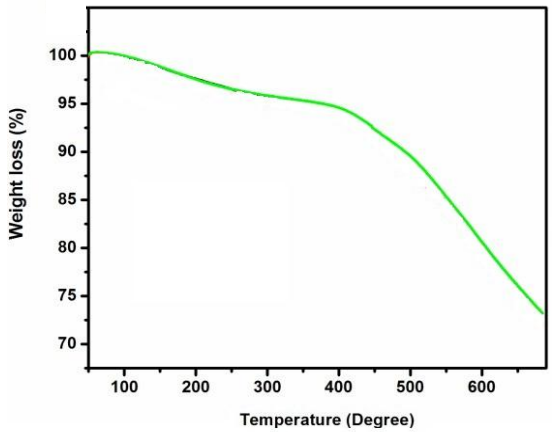

Figure 2.7: TGA curve of $SrFe_{12}O_{19}$-LLDPE nanocomposite

Saturation Magnetization

The magnetic field (B) or magnetic induction is given by (in cgs units);

$$B = H + 4\pi M_s \tag{2.5}$$

where, M_s is the magnetization produced when magnetic field H is applied to the material.

Magnetic properties of the nanoparticles are characterized by using vibrating sample magnetometer (VSM, LakeShore Model 7410) by performing magnetic hysteresis loops (M-H) at room temperature of $SrFe_{12}O_{19}$ nanoparticles sintered at 850°C as shown in figure 2.8.

Magnetization properties of the nano-composites are studied at room temperature using Pulsed Field Magnetometer developed at RRCAT, Indore, India. The saturation magnetization measurements are carried out for $SrFe_{12}O_{19}$-LLDPE composites. The applied field is 2.5 kOe. The saturation magnetization values of the composites are given in table 2.2.

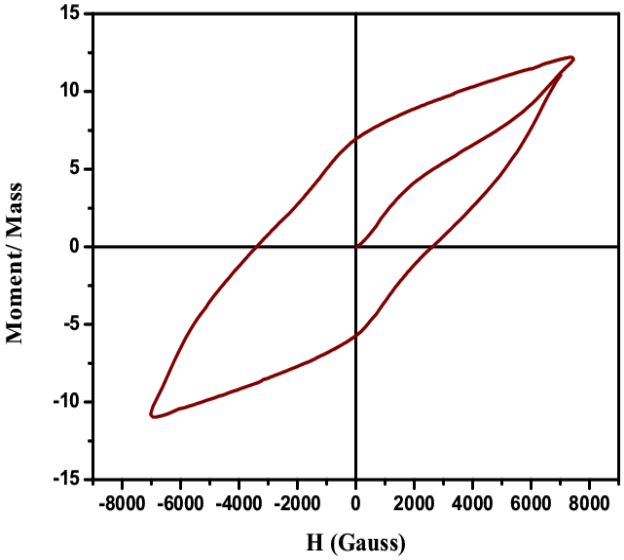

Figure 2.8: Hysteresis loop of $SrFe_{12}O_{19}$ nanoparticles sintered at 850°C

It is seen that saturation magnetization increases with increase in wt. % of the $SrFe_{12}O_{19}$ in LLDPE composite. The saturation magnetization of the composite is due to the net magnetic moment which depends on the wt. % of magnetic filler in the composite [20].

Table 2.2: Density, water absorbance and saturation magnetization of $SrFe_{12}O_{19}$-LLDPE composite with varying wt. %

wt. %	Density (g/cc)	Water absorbance (%)	$4\pi M_s$ (G)
0 wt.%	0.93	0.01	-
10 wt.%	1.10	0.01	84
20 wt.%	1.12	0.01	90
30 wt.%	1.16	0.01	99
40 wt.%	1.24	0.02	106
50 wt.%	1.30	0.02	117
60 wt.%	1.36	0.03	128
70 wt.%	1.41	0.05	133

2.3 Microwave characterization of the developed composites

Relative permittivity ($\varepsilon_r = \varepsilon_r^{'} - j\varepsilon_r^{''}$) & permeability ($\mu_r = \mu_r^{'} - j\mu_r^{''}$) measurements for all the wt. % of $SrFe_{12}O_{19}$-LLDPE nano-composite are carried out in the frequency range of 8.2-12.4 GHz.

2.3.1 Nicolson-Ross Technique for determination of complex permittivity and permeability

Nicolson-Ross technique is a non-resonant, broad band technique based on transmission/reflection method [11, 21-28]. Figure 2.9 shows the measurement configuration for a transmission/reflection method. Let Z_0 be the characteristic

impedance. A rectangular cuboid shaped sample of thickness, t is inserted into a segment of transmission line.

The new characteristic impedance of the segment with the sample is Z, given as,

$$Z=\sqrt{\mu_r/\varepsilon_r}\,Z_0 \tag{2.6}$$

where, relative permeability and permittivity, μ_r and ε_r, respectively of the material are complex quantities.

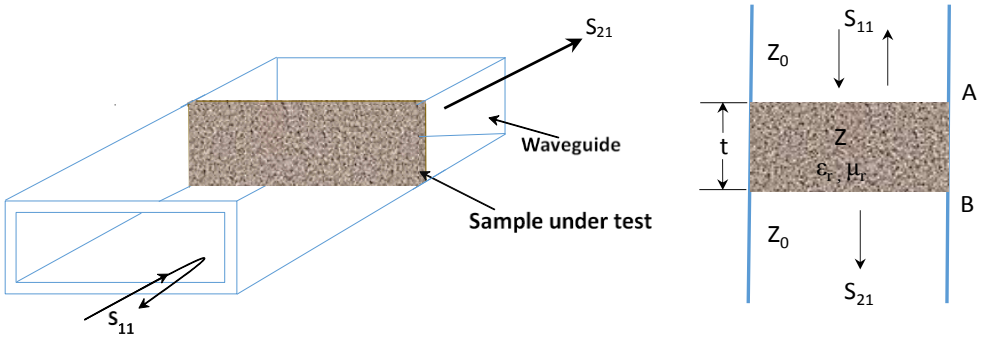

Figure 2.9: (a) Sample inside a waveguide

(b) A schematic diagram of transmission/reflection method with rectangular shape material inserted

For $t\rightarrow\infty$, the reflection coefficient, Γ, at the air-sample interface A is given as;

$$\Gamma=\frac{Z-Z_0}{Z+Z_0}=\frac{\sqrt{\frac{\mu_r}{\varepsilon_r}}-1}{\sqrt{\frac{\mu_r}{\varepsilon_r}}+1} \tag{2.7}$$

If t is finite, the transmission coefficient, T, through the segment AB is given as

$$T=exp\left[-j\left(\frac{\omega}{c}\right)\sqrt{\mu_r\varepsilon_r}t\right] \tag{2.8}$$

where, $\omega=2\Pi f$, f and c being the frequency of operation and speed of light in free space.

The scattering coefficient S_{21} and S_{11} are given by the following relations;

$$S_{21}(\omega)=\frac{(1-\Gamma^2)T}{1-\Gamma^2T^2} \tag{2.9}$$

$$S_{11}(\omega)=\frac{(1-\mathrm{T}^2)\Gamma}{1-\Gamma^2T^2} \tag{2.10}$$

Let

$$X=\frac{1-V_1V_2}{V_1-V_2} \tag{2.11}$$

where,

$$V_1 = S_{21} + S_{11} \tag{2.12}$$

$$V_2 = S_{21} - S_{11} \tag{2.13}$$

Using equations (2.9)-(2.13),

$$\Gamma = X \pm \sqrt{X^2 - 1} \tag{2.14}$$

For equation (2.14), the appropriate sign is chosen so that $|\Gamma| \leq 1$.

Similarly, using equations (2.9)-(2.13),

$$T = \frac{V_1 - \Gamma}{1 - V_1 \Gamma} \tag{2.15}$$

Rearranging equation (2.7), gives

$$\frac{\mu_r}{\varepsilon_r} = \left(\frac{1+\Gamma}{1-\Gamma}\right)^2 = c_1(say) \tag{2.16}$$

Rearranging equation (2.8), let

$$c_2 = \mu_r \varepsilon_r = -\left[\frac{c}{\omega d} \ln\left(\frac{1}{T}\right)\right]^2 \tag{2.17}$$

From equations (2.16) and (2.17),

$$\varepsilon_r = \sqrt{\frac{c_2}{c_1}} \tag{2.18}$$

$$\mu_r = \sqrt{c_1 c_2} \tag{2.19}$$

Right-hand side of equations (2.18) and (2.19) are complex terms. Separating real and imaginary parts, the complex permittivity and permeability values can be obtained.

The schematic of the measurement set up for characterization of permittivity and permeability in the X-band is shown in figure 2.10 (a). The setup consists of a vector network analyzer (Agilent E8362C), Agilent WR-90 X11644A and an interfacing computer to acquire the data. Figure 2.10 (b) shows the photograph of the measurement set-up.

The system is calibrated using thru–reflect–line (TRL) method [29, 30]. The schematic of which is shown in figure 2.11.

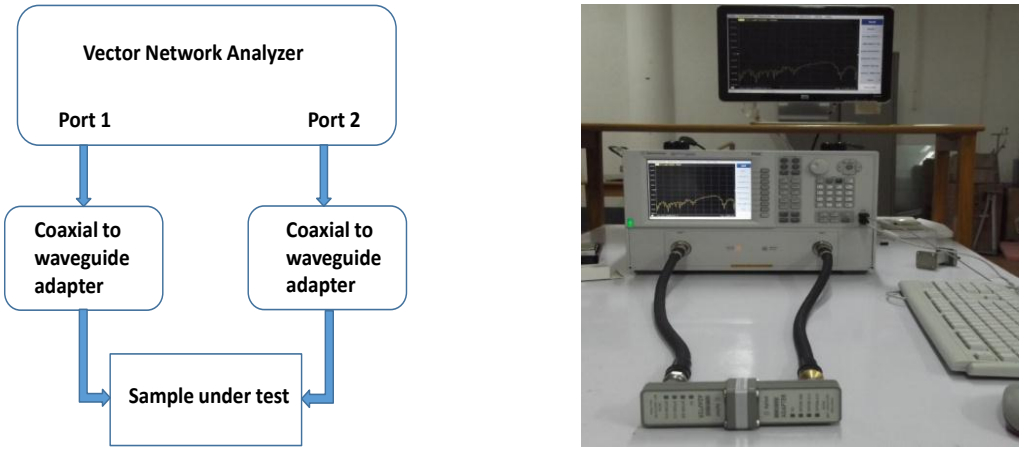

Figure 2.10: (a) Block diagram

(b) Measurement set up of X-band microwave characterization set up using transmission/reflection technique

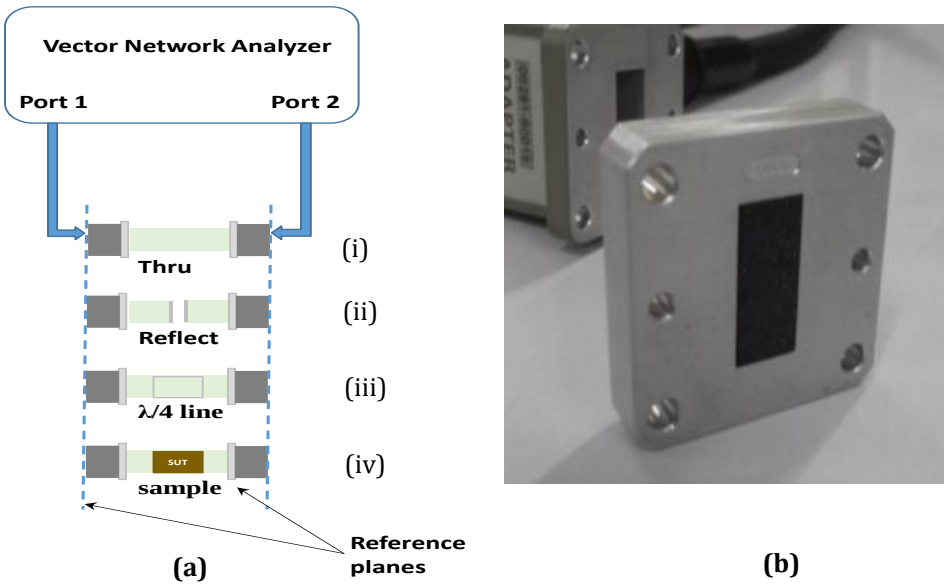

Figure 2.11: TRL calibration using Agilent WR90-X11644A calibration kit

(a) Thru /Reflect/ Line-calibration/Sample under test and

(b) X-band flange filled with sample of ferrite-LLDPE composite

In the thru calibration, the two ports are connected directly at the desired reference plane, whereas, for reflect calibration, the ports are terminated with shorts (figures 2.11 (i) and 2.11 (ii)). The two ports are then connected to a quarter wavelength segment for in line calibration (figure 2.11 (iii)). After TRL calibration, the composite of dimension 10.38 mm x 22.94 mm x t mm (t = 1, 2, 3…) is inserted into the sample holder of length 9.78 mm (shown in figure 2.11 (iv)) and mounted

on the zero reference plane i.e. at the adapter of port 1. The measured scattering parameters (S_{11} and S_{21}) are transformed to the sample edges as described in reference [11].

The transformed S_{11} & S_{21} parameter are substituted in the equations (2.6) to (2.14) to determine the complex permittivity and permeability of the composites using Agilent 85071E material measurement software employing Nicolson-Ross method. The complex permittivity and permeability values of the composites with $SrFe_{12}O_{19}$ nanoparticles as the ferrite inclusions in LLDPE matrix are measured in the frequency range of 8.2-12.4 GHz.

Results and analysis of complex permittivity and permeability of the $SrFe_{12}O_{19}$-LLDPE nano-composites

The frequency plots of ε_r' and dielectric loss tangent, $tan\ \delta_\varepsilon \left(=\frac{\varepsilon_r''}{\varepsilon_r'}\right)$ for different wt. % over the X-band are plotted in figures 2.12 (a)-(b) which do not show any significant variation with frequency. An increase in ε_r' from ~3.8 to 6.4 is observed as the amount of filler increases from 10 wt. % to 70 wt. %. Polarization in ferrites is mainly due to the interfacial polarization and intrinsic electric dipole polarization of Fe^{2+} ions. Increase in the quantity of ferrite increases easily polarizable Fe^{2+} ions, thus increasing the overall dielectric constant with increase in ferrite inclusions [13, 14]. The $tan\ \delta_\varepsilon$ values show an increase upto 60 wt. % from 0.03 to 0.4. The larger grain size of nano sized strontium ferrite sintered at 850°C contributes to dielectric losses because of localized electron hopping [31]. With further increase in filler content, a decreasing trend is observed. The $tan\ \delta_\varepsilon$ values show an increase upto 60 wt. % from 0.03 to 0.4. The larger grain size of nano sized strontium ferrite sintered at 850°C contributes to dielectric losses because of localized electron hopping [31]. With further increase in filler content, a decreasing trend is observed. The $SrFe_{12}O_{19}$-LLDPE composite consists of high permittivity nano-ferrite particles embedded in low permittivity LLDPE matrix. For lower concentration of $SrFe_{12}O_{19}$ particles, the electric field lines can pass either through polymer, path 1 (figure 2.13 (a)) or through $SrFe_{12}O_{19}$-polymer-$SrFe_{12}O_{19}$ path 2 (figure 2.13 (b)). With increase in filler concentration, there is a likelihood of the field lines taking path 3 as shown in figure 2.13 (c). Further enhancement of filler in the matrix may lead to a direct path for the field flux through the $SrFe_{12}O_{19}$ particles (figure 2.13 (d)).

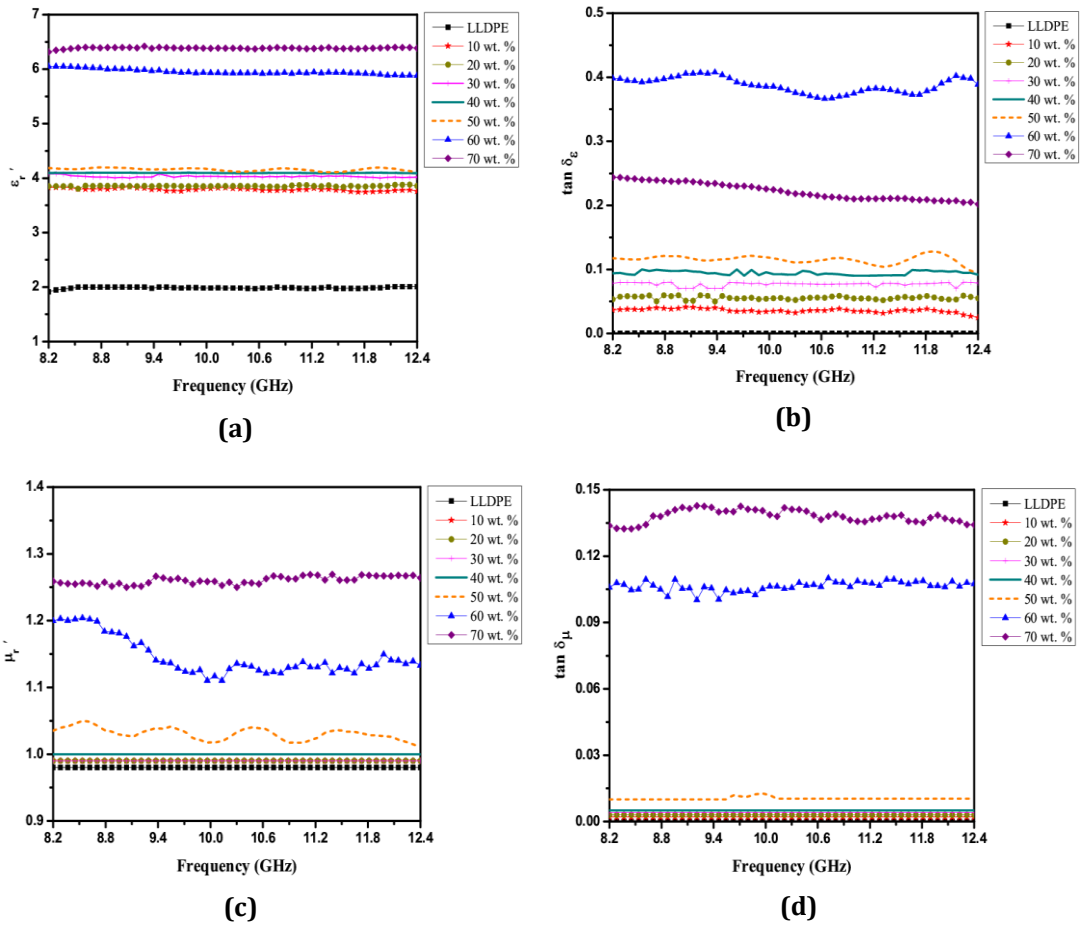

Figure 2.12: (a) Real part of complex permittivity (ε'_r),

(b) Dielectric loss tangent ($tan\ \delta_\varepsilon$),

(c) Real part of complex permeability (μ_r'),

(d) Magnetic loss tangent ($tan\ \delta_\mu$) for 10 wt. % to 70 wt. % of $SrFe_{12}O_{19}$-LLDPE nano-composite

The high value of permittivity of strontium ferrite as compared to LLDPE, clusters the flux lines into the filler particles as the rf electric field passes through a heterogeneous system of permittivities. Interfacial theory of polarization, the relatively free to move polymer chain gets restricted due to the formation of surface bonds with the inclusion surfaces restricting free movement of *em* wave through the composite. This in general leads to non-uniform electric field distribution [32, 33]. So, an increase in permittivity is observed up to 50 wt. % because of increase in following of path 1 over path 2. From 50 to 60 wt. % the discontinuity in the flow of electric flux enhances due to increase in the interfacial boundaries between $SrFe_{12}O_{19}$-LLDPE as the flux lines may follow path 3 (c) more than 1(b), which is observed with escalated increase of real and imaginary part of permittivity. Beyond 60 wt. %, the *em* wave faces less constraints due to possible overlaps of filler

particles, thus reducing the interfacial boundaries and tunnelling the electrons directly through the filler particles as seen in path 4 (d). This effect is reflected in both the real part as well as imaginary part of permittivity.

This can also explain the fact that the percentage increase of ε_r' from 50 to 60 wt. % is about 42% whereas it is only about 3.33% when the wt. % of strontium ferrite increases from 60 to 70. A similar trend is observed for imaginary part of permittivity with enhancement of loss from 50 wt. % to 60 wt. % while a decrease from 60 wt. % to 70 wt. %.

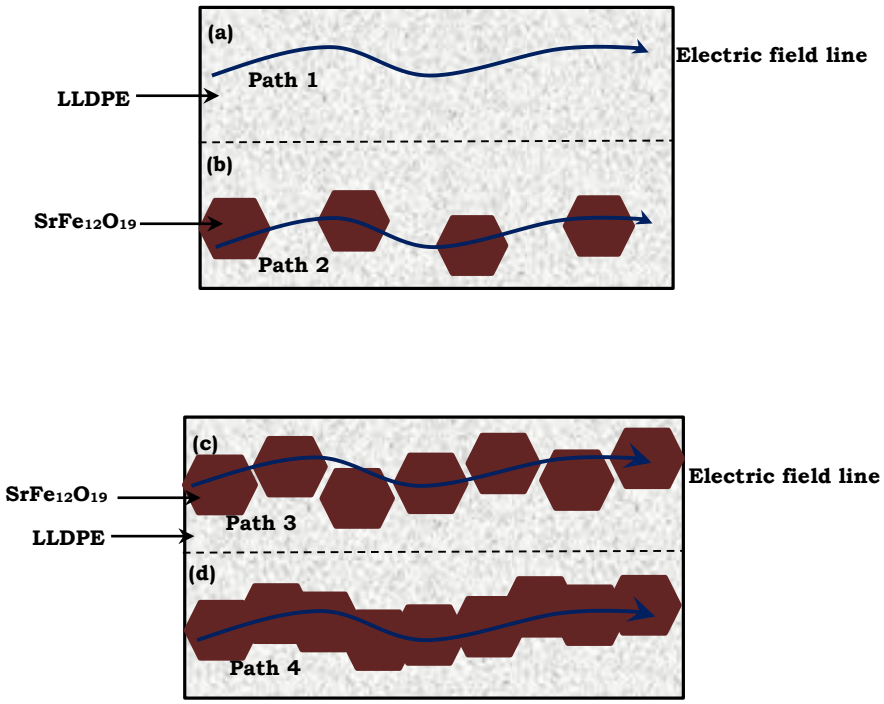

Figure 2.13: Schematic diagram of em wave propagation within the composite system

The frequency plots for μ_r' and magnetic loss tangent, $tan\ \delta_\mu \left(= \frac{\mu_r''}{\mu_r'}\right)$ for 10 wt. % to 70 wt. % of $SrFe_{12}O_{19}$-LLDPE nano-composite is given in figure 2.12 (c)-(d). μ_r' and $tan\ \delta_\mu$ show a similar trend as for ε_r' and $tan\ \delta_\varepsilon$, respectively, not showing much variation with frequency. With increase in filler content μ_r' increases from 0.98 to 1.26 while $tan\ \delta_\mu$ changes from 0.003 to 0.142. The dispersion of complex permeability in a magneto-dielectric polymer composite is primarily due to the resonance of oscillating domain walls and the resonance of magnetic moments in domains which is known as natural ferromagnetic resonance [3, 34, 35]. For single domains, the domain wall oscillations do not occur, and hence the permeability of the ferrite can be attributed to the resonance

phenomenon. The ferromagnetic resonance frequency (f_r) follows the relation, $f_r = \frac{\gamma}{2\pi} H_a$, where γ is the gyromagnetic ratio and H_a is the anisotropy field. Also, it is reported that strontium ferrite shows natural resonance peak at high microwave frequencies [36]. The main contributing factors for magnetic losses is the high anisotropy of the M-type strontium ferrite [3]. Thus, with increase in the weight percentage of $SrFe_{12}O_{19}$ in the composite the overall permeability increases accordingly.

Suitability of $SrFe_{12}O_{19}$-LLDPE nano-composites for absorber design

Due to the high values of permittivity, permeability as well as both dielectric and magnetic losses, $SrFe_{12}O_{19}$-LLDPE nano-composites are suitable material for absorber design. The composite remains light weight as the density increases only marginally with increase in filler percentage up to 70 wt. %. Performance of absorbers using these nano-composites can be expected to be unaffected by moisture as water absorbance is found to be negligible. The nanosized strontium ferrite blends uniformly in LLDPE matrix assuring uniform propagation of electromagnetic wave in all directions. All the composites from 10 wt. % to 70 wt. % are designed and studied as single layer absorbers and are presented in the following section.

2.4 Design of a single layer absorber using transmission line model

Plane electromagnetic waves propagating in bulk slabs can be modeled by transmission line equations [37-40]. Numerical technique is applied for analysing wave propagation in the absorber based on TL model using temporal and spatial sampling of electromagnetic fields. The transmission lines are simulated as propagation domain, where the electric and magnetic vectors of propagating electromagnetic wave are made equivalent to voltages and currents on the network respectively.

2.4.1 TL model for a single layer absorber

A transmission line carrying TEM wave is represented as distributed elements in a network having series impedance $Z = R + j\omega L$ and shunt admittance $Y = G + j\omega C$ per unit length [41, 42] as shown in figure 2.14.

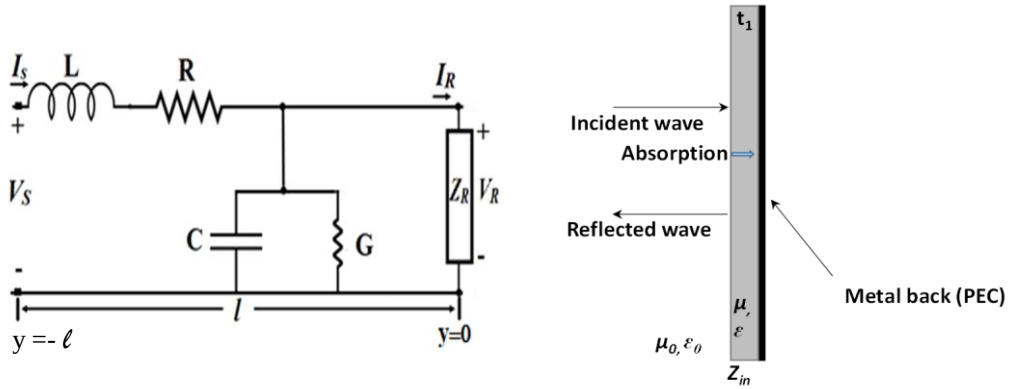

Figure 2.14: (a) A circuit representation of a transmission line
(b) A metal-backed single layer absorber

The voltage and current distribution along the transmission line are functions of both time and position and are mainly determined from properties of the conductors and dielectrics [19].

For a uniform transmission line having the constants *R*, *L*, *C* and *G* per unit length, the voltage and current equations can be written in the differential form as;

$$\frac{\partial \tilde{V}}{\partial y} + L\frac{\partial \tilde{I}}{\partial t} + R\tilde{I} = 0 \tag{2.20}$$

$$\frac{\partial \tilde{I}}{\partial y} + C\frac{\partial \tilde{V}}{\partial t} + G\tilde{V} = 0 \tag{2.21}$$

If the voltages and currents vary sinusoidally with time, the phasor notation of equations (2.20) and (2.21) become;

$$\frac{\partial V}{\partial y} + (R + j\omega L)I = 0 \tag{2.22}$$

$$\frac{\partial I}{\partial y} + (G + j\omega C)V = 0 \tag{2.23}$$

The analogous relation between electric and magnetic field components of plane wave to the transmission line parameters are given as $\frac{\partial E_z}{\partial y} + j\omega\mu H_x = 0$ and $\frac{\partial H_x}{\partial y} + (\sigma_s + j\omega\varepsilon)E_z = 0$.

Differentiating equations (2.22) and (2.23) with respect to *x* and combining gives;

$$\frac{\partial^2 V}{\partial y^2} - (R + j\omega L)(G + j\omega C)V = 0 \tag{2.24}$$

$$\frac{\partial^2 I}{\partial y^2} - (R + j\omega L)(G + j\omega C)I = 0 \tag{2.25}$$

A possible solution for these equations would be of the form

$$V \text{ or } I = Ae^{-\gamma y} + Be^{\gamma y} \tag{2.26}$$

where, $\gamma^2 = (R + j\omega L)(G + j\omega C)$ (2.27)

When the variation with time is expressed explicitly, the first term of the expression (2.26) represents a wave travelling in forward direction and the second term represents a wave travelling in reverse direction.

In hyperbolic function form, the solutions to equations (2.24) and (2.25) are

$$V = A_1 cosh\, \gamma y + B_1 sinh\, \gamma y \tag{2.28}$$

$$I = A_2 cosh\, \gamma y + B_2 sinh\, \gamma y \tag{2.29}$$

Considering the location of the terminating impedance Z_R the reference point (y = 0), the other end is left of this reference point, i.e. in the –y direction as shown in figure 2.14 (a). Solving the constants, A_1, B_1, A_2 and B_2 and writing $l = -y$, equations (2.28) and (2.29) becomes

$$V_S = V_R cosh\, \gamma l + Z_0 I_R\, sinh\, \gamma l \tag{2.30}$$

$$I_S = I_R cosh\, \gamma l + \frac{V_R}{Z_0} sinh\, \gamma l \tag{2.31}$$

The general expression for the input impedance of the transmission line is obtained by dividing equation (2.30) by equation (2.31) i.e.

$$Z_{in} = \frac{V_S}{I_S} = \frac{V_R cosh\, \gamma l + Z_0 I_R\, sinh\, \gamma l}{I_R cosh\, \gamma l + \frac{V_R}{Z_0} sinh\, \gamma l} \tag{2.32}$$

or

$$Z_{in} = Z_0 \frac{Z_R + Z_0 tanh\, \gamma l}{Z_0 + Z_R tanh\, \gamma l} \tag{2.33}$$

The expression (2.33) gives the input impedance of the transmission line terminated by a load, Z_R. The input impedance of a single layer absorber can be expressed as,

$$Z_{in} = Z_0 tanh\left[j\left({}^{2\pi ft}/_{c}\right)\sqrt{\mu_r \varepsilon_r}\right] \tag{2.34}$$

where, ε_r *(=* ε_r'*-j*ε_r''*),* is the complex permittivity, μ_r *(=* μ_r'*-* $j\mu_r''$*)*,the complex permeability, *t*, thickness of the absorber and *f*, the incident microwave frequency [34]. The reflection coefficient is expressed as

$$\Gamma = \frac{Z_{in} - Z_0}{Z_{in} + Z_0} \tag{2.35}$$

The reflection loss, *RL*, for a single layer absorber is given by

$$RL = 20\log\left|\frac{Z_{in}-Z_0}{Z_{in}+Z_0}\right| \quad (2.36)$$

Equation (2.36) can be rewritten as

$$RL = 20\log\left|\frac{\sqrt{\mu_r/\varepsilon_r}tanh[(j2\pi f/c)\sqrt{\mu_r/\varepsilon_r}t]-1}{\sqrt{\mu_r/\varepsilon_r}tanh[(j2\pi f/c)\sqrt{\mu_r/\varepsilon_r}t]+1}\right| \quad (2.37)$$

2.5 Absorption studies

Theoretical computation of reflection loss of 10 to 70 wt. % $SrFe_{12}O_{19}$-LLDPE nano-composites are carried out for thickness optimization in each composition. Based on the computed results, a single layer metal backed absorber is fabricated and tested for microwave absorption over the X-band.

2.5.1 Computed microwave absorption using TLM

The thickness of the absorber sample is varied from 1 mm to 4 mm in steps of 0.5 mm for 10 wt. % to 70 wt. % $SrFe_{12}O_{19}$-LLDPE nano-composites.

Table 2.3: Calculated reflection loss (RL_c) of $SrFe_{12}O_{19}$-LLDPE nano-composites with varying thickness and wt. % from 10 wt. % to 70 wt. % using TL model

t (mm)	10 wt.%		20 wt.%		30 wt.%		40 wt.%		50 wt.%		60 wt.%		70 wt.%	
	RL_c (dB)	f_r (GHz)	RL_c (dB)	f_r (GHz)	RL_c (dB)	f_r (GHz)	RL_c (dB)	f_r (GHz)	RL_c (dB)	f_r (GHz)	RL_c (dB)	f_r (GHz)	RL_c (dB)	f_r (GHz)
1.0	-0.10	12.4	-0.15	12.4	-0.17	12.4	-0.16	12.4	-0.17	12.4	-1.0	12.4	-0.40	12.4
1.5	-1.24	12.4	-1.36	12.4	-1.29	12.4	-1.62	12.4	-1.90	12.4	-4.5	12.4	-1.78	12.4
2.0	-1.32	12.4	-1.43	12.4	-1.26	12.4	-1.38	12.4	-1.98	12.4	-13.5	12.4	-6.50	12.4
2.5	-1.41	12.4	-1.28	12.4	-1.34	12.4	-1.95	12.4	-2.56	12.4	-40.4	12.1	-16.40	12.4
3.0	-1.46	10.3	-1.51	10.2	-1.53	10.5	-2.84	10.3	-6.59	10.3	-40.2	10.5	-18.80	11.2
3.5	-1.09	9.5	-1.16	9.5	-1.46	9.1	-1.98	9.1	-2.30	9.0	-49.6	9.0	-23.00	8.2
4.0	-1.11	9.1	-1.24	8.2	-1.30	8.2	-1.86	8.2	-1.15	8.2	-40.0	8.2	-22.00	8.2

Table 2.3 shows the calculated reflection loss (RL_c) values with varying thickness of the composite. Corresponding resonant frequency (f_r) is also included. From table 2.3 it is observed that 10 wt. % to 50 wt. % $SrFe_{12}O_{19}$-LLDPE nano-composites do not show significant reflection loss. 60 wt. % and 70 wt. % of $SrFe_{12}O_{19}$-LLDPE composite, however, show appreciable reflection loss.

From Fig. 2.12 (a-d), referring to the values of ε_r', μ_r' and loss tangent spectra, the real part of complex permittivity and permeability for these two weight fractions show higher values than the rest of the compositions and the losses are also relatively high. As significant improvement in absorption is seen when the wt. %

increases from 50 wt. % to 60 wt. %, samples with 55 wt. % and 65 wt. % are also fabricated & characterized. The real part of the complex permittivity, ε_r' & $tan\ \delta_\varepsilon$ for 55, 60, 65 & 70 wt. % of the $SrFe_{12}O_{19}$-LLDPE nano-composite over the X-band are plotted in figure 2.15 (a)-(b). The frequency plots for the real part of the complex permeability, μ_r', and $tan\ \delta_\mu$ for 55, 60, 65 and 70 wt. % of nano-composite are given in figure 2.15 (c)-(d). 65 wt. % and 70 wt. % composites show lower values of dielectric loss which is explained by the interfacial theory of polarization and the tunneling theory mentioned earlier.

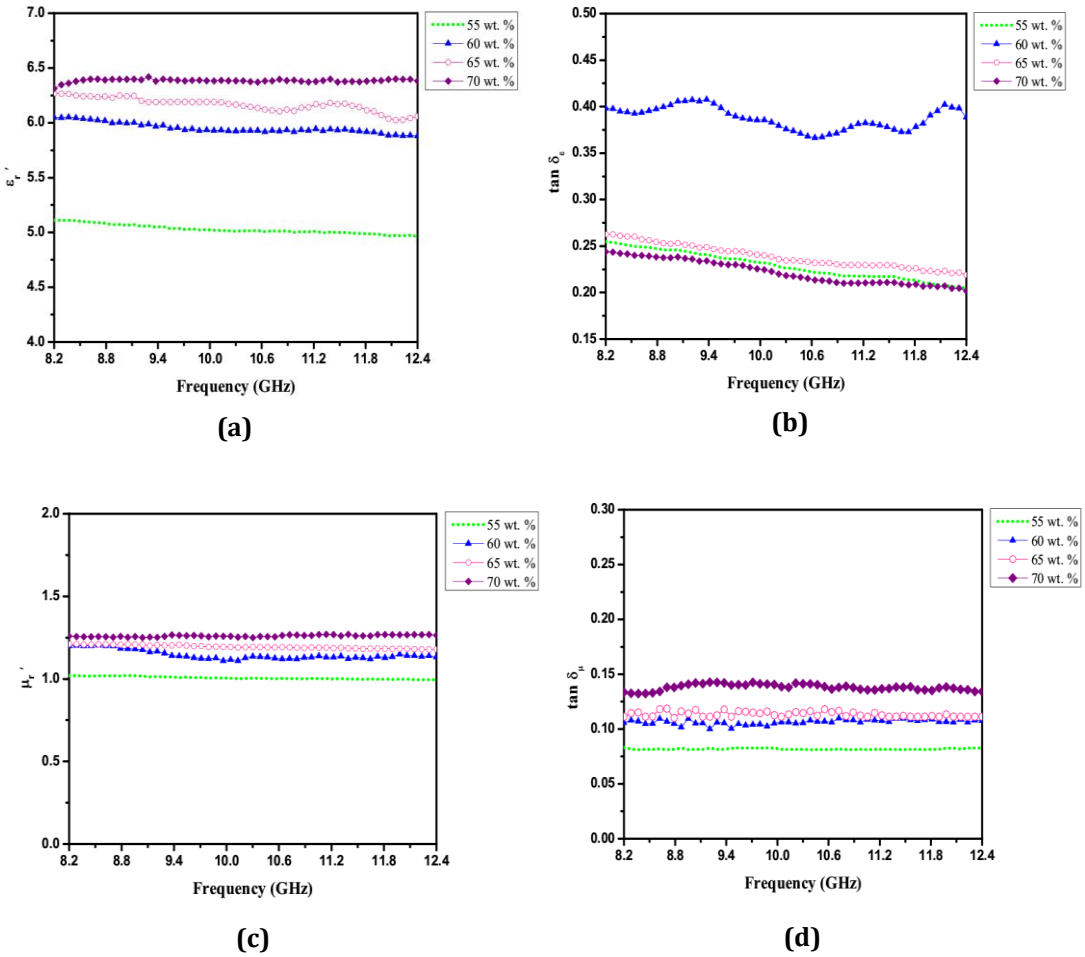

Figure 2.15: (a) Real part of complex permittivity (ε'_r),

(b) Dielectric loss tangent ($tan\ \delta_\varepsilon$),

(c) Real part of complex permeability (μ_r'),

(d) Magnetic loss tangent ($tan\ \delta_\mu$) for 55 wt. %, 60 wt. %, 65 wt. % and 70 wt. % of $SrFe_{12}O_{19}$-LLDPE nano-composite

Using equation (2.34), complex input impedance, Z_{in}, is calculated. Figures 2.16-2.19 show the plots of real (Z_{in}') and imaginary (Z_{in}'') values of input

impedance for 55 wt. % to 70 wt. %. It is observed that the input impedance for all the percentages matches the free space impedance values for t = 3mm.

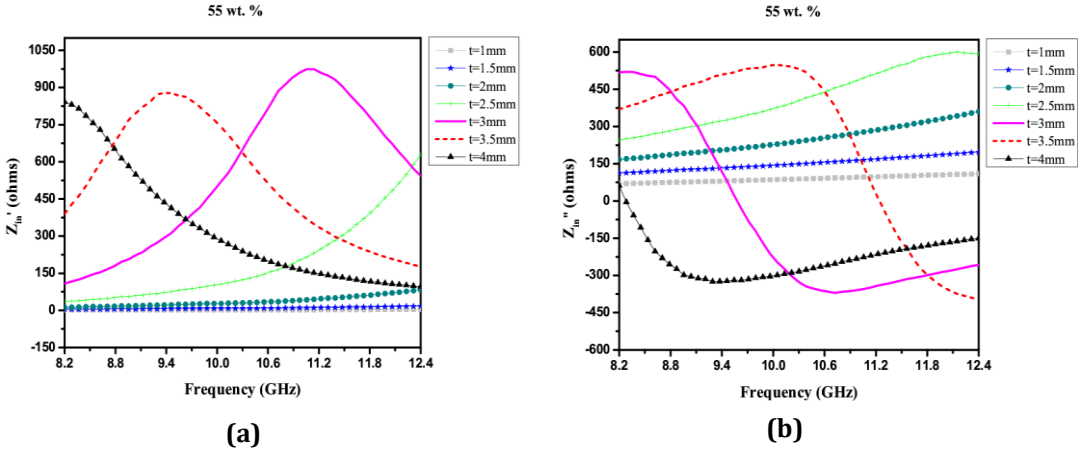

Figure 2.16: Calculated input impedance for t=1 mm to 4 mm, 55 wt. % of $SrFe_{12}O_{19}$-LLDPE nano-composite

(a) Real part of input Impedance (Z_{in}'),

(b) Imaginary part of input Impedance (Z_{in}'')

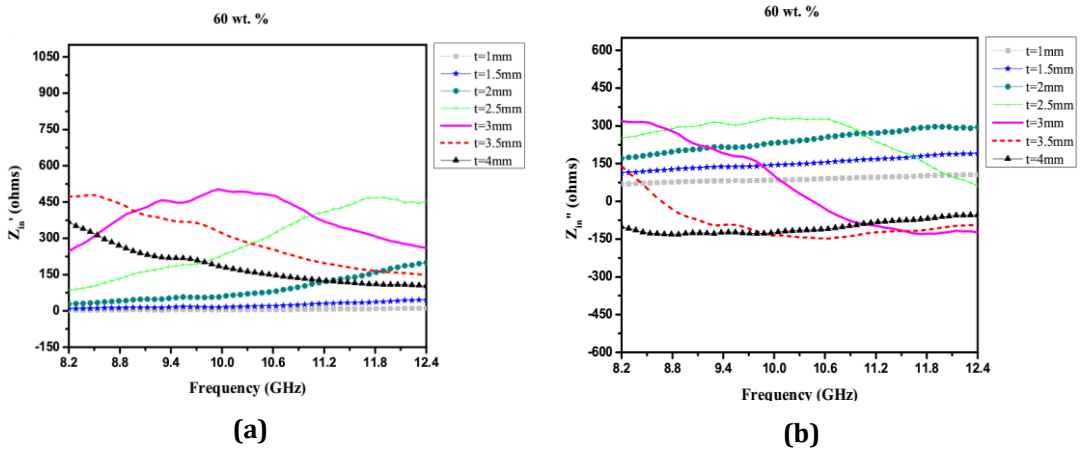

Figure 2.17: Calculated input impedance for t=1 mm to 4 mm, 60 wt. % of $SrFe_{12}O_{19}$-LLDPE nano-composite

(a) Real part of input impedance (Z_{in}'),

(b) Imaginary part of input impedance (Z_{in}'')

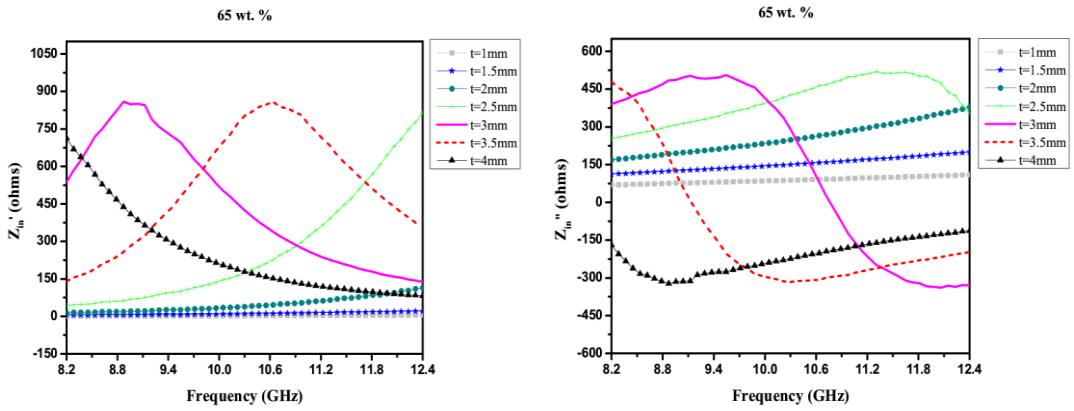

(a) **(b)**

Figure 2.18: Calculated input impedance for t=1 mm to 4 mm, 65 wt. % of $SrFe_{12}O_{19}$-LLDPE nano-composite

(a) Real part of input impedance (Z_{in}'),

(b) Imaginary part of input impedance (Z_{in}'')

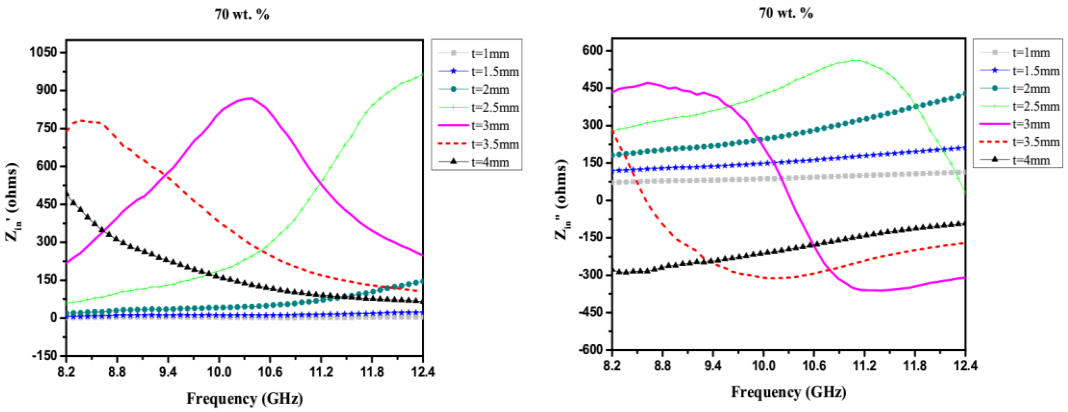

(a) **(b)**

Figure 2.19: Calculated input impedance for t=1 mm to 4 mm, 70 wt. % of $SrFe_{12}O_{19}$-LLDPE nano-composite

(a) Real part of input impedance (Z_{in}'),

(b) Imaginary part of input impedance (Z_{in}'')

RL_c is determined using equation (2.37) for different thicknesses of the absorber for 55, 60, 65 and 70 wt. % composite over the X-band and figure 2.20 gives the values of RL_c for $SrFe_{12}O_{19}$-LLDPE composites with thickness varying from 1 mm to 4 mm. The results are given in table 2.4.

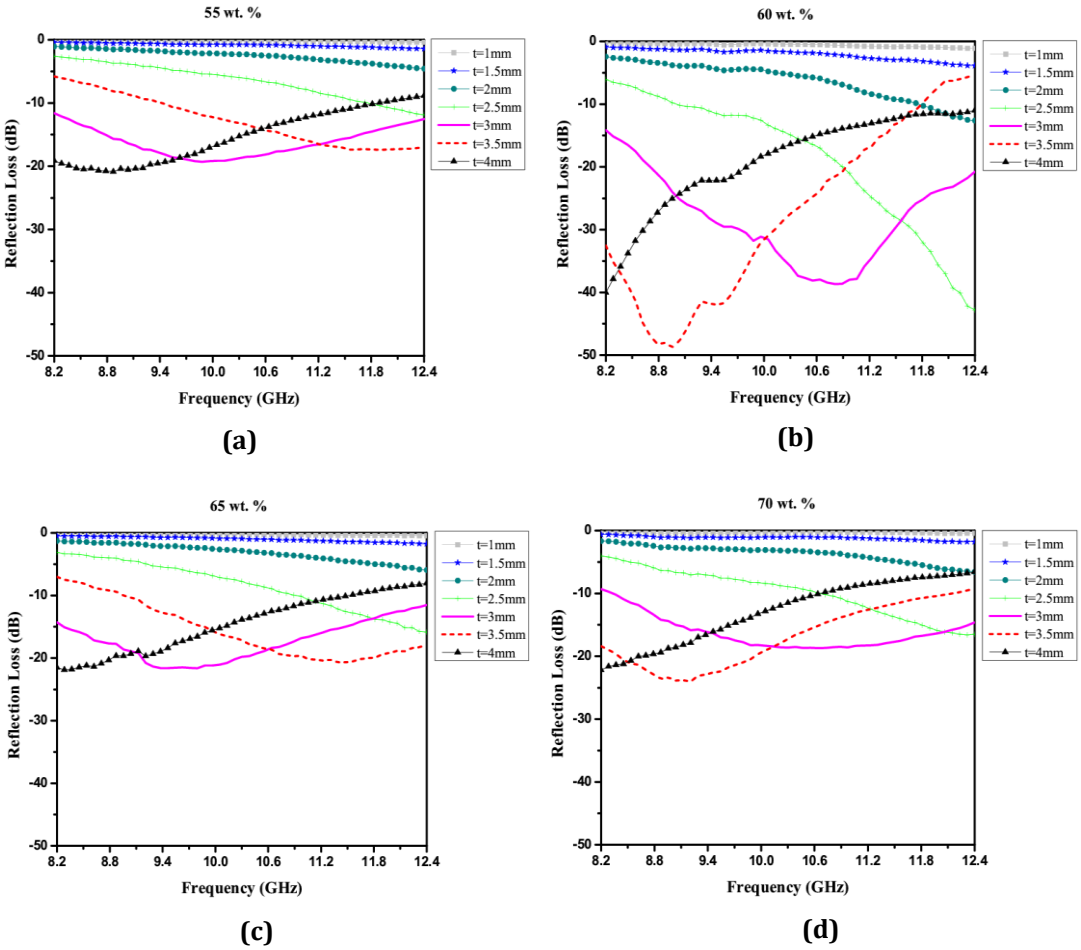

Figure 2.20: *RL*$_c$ of $SrFe_{12}O_{19}$-LLDPE composite with thickness varying from 1mm to 4mm **(a)** 55 wt. % **(b)** 60 wt. % **(c)** 65 wt. % **(d)** 70 wt. % (Calculated)

From the plots in figure 2.20, it is observed that the -10 dB calculated absorption bandwidth (BW_c) is better for $t \geq 2.5$ mm for all wt. % as compared to those for $t < 2.5$ mm. 60 wt. % composites with $t = 3$ mm shows a maximum -10 dB absorption bandwidth as well as peak RL value. It is interesting to see that the corresponding real (Z_{in}') and imaginary (Z_{in}'') values of the input impedance are together closest to the free space real and imaginary impedance values of 377 Ω and 0 Ω, respectively, for all the wt. percentages that are fabricated.

Single layer sheets of thickness, $t = 3$ mm & dimension 10.38 mm x 22.94 mm are fabricated using $SrFe_{12}O_{19}$-LLDPE composites with wt. % of 55, 60, 65 and 70. The sample is placed inside an X-band sample holder (WR-90 X11644A) of length 97.8 cm mounted on the zero reference plane terminated by a short. S_{11} parameter is measured in the frequency range of 8.2-12.4 GHz.

Table 2.4: Input impedance (real and imaginary), calculated reflection loss (RL_c) of $SrFe_{12}O_{19}$-LLDPE composite with varying t & wt. % from 55 wt. % to 70 wt. % using TL Model

$SrFe_{12}O_{19}$-LLDPE	t (mm)	Z_{in}'(Ω)	Z_{in}''(Ω)	RL_c (dB)	f_r (GHz)	-10 dB BW_c (GHz)
55 wt.%	1.0	3.82	109.78	-0.37	12.40	-
	1.5	17.21	200.00	-1.42	12.40	-
	2.0	82.73	390.20	-4.55	12.40	-
	2.5	628.30	600.62	-11.88	12.40	0.58
	3.0	380.20	-200.24	-17.08	9.37	4.20
	3.5	257.41	-237.60	-16.40	11.07	2.64
	4.0	690.40	-380.54	-20.85	8.87	2.90
60 wt.%	1.0	11.04	106.33	-1.09	12.40	-
	1.5	50.00	205.20	-3.85	12.40	-
	2.0	200.23	308.30	-12.62	12.40	0.58
	2.5	450.48	92.41	-39.40	12.40	3.36
	3.0	440.32	-1.91	-39.70	10.30	4.20
	3.5	402.34	-67.63	-48.60	8.87	3.52
	4.0	390.64	-101.06	-39.00	8.20	4.20
65 wt.%	1.0	4.42	109.20	-0.43	12.40	-
	1.5	20.94	200.46	-1.73	12.40	-
	2.0	114.64	383.45	-5.92	12.40	-
	2.5	813.48	355.65	-15.83	12.40	1.43
	3.0	264.08	-190.78	-19.71	9.54	4.20
	3.5	708.86	-244.78	-20.00	11.39	3.40
	4.0	713.34	-169.08	-20.70	8.20	3.17
70 wt.%	1.0	4.10	113.13	-0.40	12.40	-
	1.5	22.11	212.02	-1.78	12.40	-
	2.0	145.78	410.73	-6.50	12.40	-
	2.5	964.43	230.83	-16.40	12.40	1.60
	3.0	487.70	-260.00	-18.80	11.39	4.10
	3.5	737.65	282.45	-23.00	9.20	3.78
	4.0	520.22	-277.90	-22.00	8.20	2.90

2.5.2 Measured microwave absorption

The measured reflection loss (RL_m) spectrum and calculated reflection loss (RL_c) using TLM for the same thickness t = 3 mm, for 55, 60, 65 and 70 wt. % composites in the X-band is given in figure 2.21.

The measured and calculated values of reflection loss, resonant frequency and -10 dB absorption bandwidth are given in table 2.5. From the table, it can be seen that 60 wt. % composite shows maximum RL_m of -22 dB and -10 dB absorption bandwidth (BW_m) of 3.36 GHz (8.53 GHz-11.89 GHz) amongst all the wt. %.

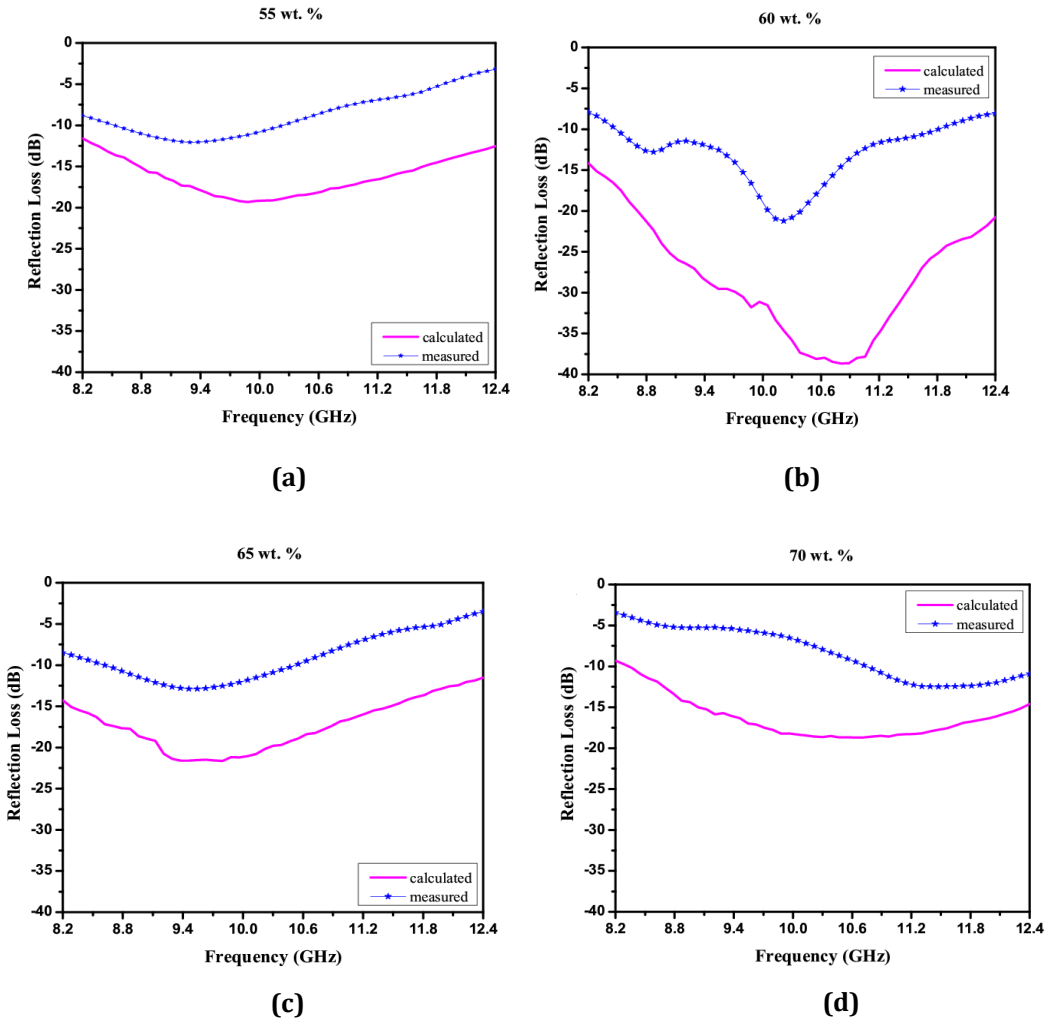

Figure 2.21: Measured and calculated *RL* of $SrFe_{12}O_{19}$-LLDPE composite with *t*= 3mm **(a)** 55 wt. % **(b)** 60 wt. % **(c)** 65 wt. % **(d)** 70 wt. %

The resonant frequency of RL_m and RL_c are in close proximity; the small shift in frequency could be due to fabrication tolerance. The transmission line model used to calculate reflection loss having its attendant approximations, gives loss estimations generally on the higher side as compared to measured results [13]. Practically, the absorber is designed for specific thickness satisfying the condition of destructive interference at a particular frequency.

Table 2.5: RL, -10 dB absorption bandwidth and resonant frequency for 55, 60, 65 and 70 wt. % of $SrFe_{12}O_{19}$-LLDPE for *t* = 3mm

$SrFe_{12}O_{19}$-LLDPE	Measured			Calculated		
	RL_m (dB)	f_{rm} (GHz)	-10 dB BW_m (GHz)	RL_c (dB)	f_{rc} (GHz)	-10 dB BW_c (GHz)
55 wt.%	-12.07	9.40	1.6	-17.08	9.37	4.2
60 wt.%	-22.19	10.20	3.3	-39.70	10.30	4.2
65 wt.%	-12.87	9.46	1.9	-19.71	9.54	4.2
70 wt.%	-12.48	11.30	0.6	-18.80	11.39	4.1

The attenuation constant (α) of the $SrFe_{12}O_{19}$-LLDPE composite is determined using equation (1.16) from the measured complex permittivity (ε_r) and complex permeability (μ_r) values of the composites for X-band. Figure 2.22 shows the variation of attenuation constant with frequency. The maximum attenuation is obtained for the composite with 60 wt. % of $SrFe_{12}O_{19}$-LLDPE varying from 85.0 dB/cm at 8.2 GHz to 131.5 dB/cm at 12.4 GHz over the frequency range.

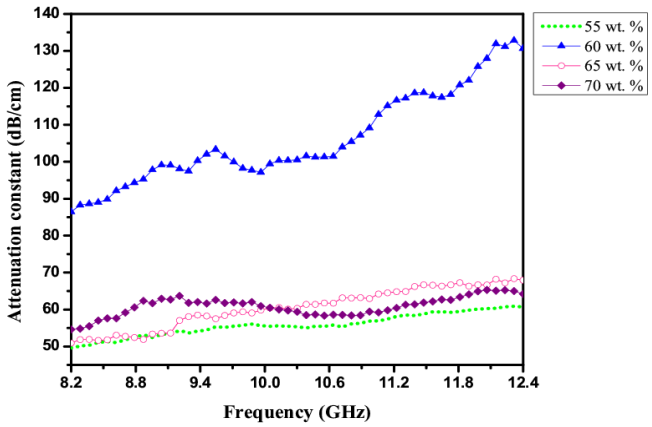

Figure 2.22: Attenuation constant of $SrFe_{12}O_{19}$-LLDPE for 55, 60, 65 and 70 wt. % for t = 3 mm

In case of 60 wt. % it is observed that the real and imaginary part of complex input impedance together is much closer to the free-space impedance then the complex input impedance values of other weight percentages (Table 2.4), leading to more penetration of the incident wave into the material. The total loss is an aggregate of dielectric and magnetic losses [43]. In the 60 wt. % composite, the dielectric loss is higher than other compositions (figure 2.15 (b)).

Absorption performance of some of the reported works, in X-band, using strontium ferrite as filler is presented in table 2.6 along with the present work.

Table 2.6: Comparison of microwave absorbing properties of recent reported single-layer absorbers

Material composition	**Thickness (mm)**	**Max RL (dB)**		**-10 dB bandwidth (GHz)**	
		Theor.	**Exp.**	**Theor.**	**Exp.**
SrF and $ZnFe_2O_4$ in paraffin wax [44]	2.2	-37.0	-	2.21	-
SrF & carbon black in nitrile rubber [45]	5.0	-	-16.0	-	2.6
$SrFe_{12}O_{19}$ in LLDPE (Present work)	3.0	-39.70	**-22.19**	4.2	**3.36**

2.7 Conclusion

In this chapter, nano sized strontium ferrite is synthesized and included in LLDPE matrix in different weight ratios. Since LLDPE as matrix doesn't allow breakdown of the bonds, filler content up to 70 wt. % can be included in the matrix. 3 mm thick single layer composite of 60 wt. % $SrFe_{12}O_{19}$-LLDPE shows -10 dB absorption bandwidth of 3.36 GHz (8.536 GHz-11.896 GHz) and maximum attenuation. Use of LLDPE also offers the added benefit of relatively lighter absorber weight and lower thickness. The prepared $SrFe_{12}O_{19}$-LLDPE absorber is resistant to water. The overall density of the developed composites do not increase significantly owing to the lower density of the synthesized nano magnetic fillers. Consequently, increase of weight of developed composite absorber does not become a concern due to the addition of strontium ferrite as filler.

For further studies, 60 wt. % composite is used in the subsequent chapters.

References:

[1] Cochardt A. (1963). Modified strontium ferrite, a new permanent magnet material. *Journal of Applied Physics*, 34: 1273–1274.

[2] Guohong M., Chen, N., Pan, X., Shen H. and Mingyuan, G. (2008). Preparation and microwave absorption properties of barium ferrite nanorods. *Material Letters*, 62: 840–842.

[3] Ghasemi A., Hossienpour, A., Morisako, A., Saatchi A. and Salehi, M. (2006). Electromagnetic properties and microwave absorbing characteristics of doped barium hexaferrite. *Journal of Magnetism and Magnetic Materials*, 302: 429–435.

[4] Li B. W., Shen, Y., Yue, Z. X. and Nan, C. W. (2007). Influence of particle size on electromagnetic behavior and microwave absorption properties of Z-type Ba-ferrite/polymer composites. *Journal of Magnetism and Magnetic Materials*, 313: 322–328.

[5] Ghasemi A., Liu, X. and Morisako, A. (2009). Effect of additional elements on the structural properties, magnetic characteristics and natural resonance frequency of strontium ferrite nanoparticles/polymer composite. *IEEE Transactions on Magnetics*, 45: 4420–4423.

[6] Ghasemi A., Sepelák, V., Liu, X. and Morisako, A. (2009). Microwave absorption properties of Mn–Co–Sn doped barium ferrite nanoparticles. *IEEE Transactions on Magnetics*, 45: 2456–2459.

[7] Saunders, K. J. *Organic Polymer Chemistry*. Chapman and Hall, 1973.

[8] Dominighaus, H. *Plastic for Engineering*. Hanser Publishers, 1988.

[9] Harper, C. A. *Handbook of Plastics Technologies*. McGraw Hill Professional, 2010.

[10] Huang, X., Liu, F. and Jiang, P. (2010). Effect of nanoparticle surface treatment on morphology, electrical and water treeing behavior of LLDPE composites. *IEEE Transaction on Dielectrics and Electrical Insulation*, 17: 1697–1704.

[11] Nicolson, A. M. and Ross, G. F. (1970). Measurement of the intrinsic properties of materials by time-domain techniques. *IEEE Transactions on Instrumentation Measurement*, IM-19: 377–382.

[12] Kakati, B. K. and Deka, D. (2007). Differences in physico-mechanical behaviors of resol (e) and novolac type phenolic resin based composite

bipolar plate for proton exchange membrane (PEM) fuel cell. *Electrochimica Acta*, 52: 7330–7336.

[13] Ozah, S. and Bhattacharyya, N. S. (2013). Nanosized barium hexaferrite in novolac phenolic resin as microwave absorber for X-band application. *Journal of Magnetism and Magnetic Materials*, 342: 92–99.

[14] Gupta N., Dimri, M. C., Kashyap, S. C. and Dube, D. C. (2005). Processing and properties of cobalt-substituted lithium ferrite in the GHz frequency range. *Ceramic International*, 31: 171–176.

[15] Mali, A. and Ataie, A. (2005). Structural characterization of nano-crystalline $BaFe_{12}O_{19}$ powders synthesized by sol–gel combustion route. *Scripta Materialia*, 53: 1065–1070.

[16] Irani, M., Ismail, H. and Ahmad, Z. (2013). Preparation and properties of linear low-density polyethylene-g-poly (acrylic acid)/ organo-montmorillonite super absorbent hydrogel composites. *Polymer Testing*, 32: 502–512.

[17] Chen, D., Meng, Y., Gandha, K. H., Zeng, D., Yu, H. and J. Ping Liu (2017). Morphology control of hexagonal strontium ferrite micro/nano-crystals. *AIP Advances*, 7: 056214-1–5.

[18] Ge, M. Y., Wu, H. P., Niu, L., Liu, J. F., Chen, S. Y., Shen, P. Y., Zeng, Y. W., Wang, Y. W., Zhang, G. Q. and Jiang, J. Z. (2007). Nanostructured ZnO: from monodisperse nanoparticles to nanorods. *Journal of Crystal Growth*, 305: 162-166.

[19] Pratten, N. A. (1981). The precise measurement of the density of small samples, *Journal of Materials Science*, 16: 1737–1747.

[20] Berkowitz A. E., Shuele, W. J. and Flanders, P. J. (1968). Influence of crystallite size on the magnetic properties of acicular γ-Fe_2O_3 particles. *Journal of Applied Physics*, 39: 1261–1263.

[21] Hajian, M., Mathew, K. T. and Ligtha, L. P. (1999). Measurement of complex permittivity with waveguide resonator using perturbation technique. *Microwave and Optical Technology Letters*, 21 (4): 269–272.

[22] Murthy, V. R. K., Sunderam, S. and Viswanathan, B. *Microwave Materials*. Narosa Publishing House, New Delhi, 1990.

[23] Chen, L. F., Ong, C. K., Neo, C. P., Varadan, V. V. and Varadan, V. K. *Microwave Electronics Measurement and Material Characterization*. John Willey and Sons, West Sussex, England, 2004.

[24] Yamashita, E., Atsuki, K. and Hirahata, T. (1981). Microstrip dispersion in a wide frequency range. *IEEE Transactions on Microwave Theory and Techniques*, 29 (6): 610–611.

[25] Yamashita, E., Atsuki, K. and Ueda, T. (1979). An approximate dispersion formula of microstrip lines for computer aided design of microwave integrated circuits. *IEEE Transactions on Microwave Theory and Techniques*, 27 (12): 1036–1038.

[26] Al-Moayed, N. N., Afsar, M. N., Khan, U. A., McCooey, S. and Obol, M. (2008). Nano ferrites microwave complex permeability and permittivity measurements by T/R technique in waveguide. *IEEE Transactions on Magnetics*, 44 (7): 1768–1772.

[27] Jarvis, J. B., Vanzura, E. J. and Kissick, W. A. (1990). Improved technique for determining complex permittivity with the transmission/reflection method. *IEEE Transactions on Microwave Theory and Techniques*, 38 (8): 1096–1103.

[28] Krupka, J. (2006). Frequency domain complex permittivity measurements at microwave frequencies, *Measurement Science and Technology*, 17: 55–70.

[29] TRL/LRM Calibration, Agilent E5070B/E5071B ENA Series RF Network Analyzers,1st Edition, Agilent Technologies, No. 16000–95026, Japan, 2004.

[30] Engen, G. F. and Hoer, C. A. (1979). Thru-reflect-line: An improved technique for calibrating the dual six-port automatic network analyser. *IEEE Transactions on Microwave Theory and Techniques*, 27 (12): 987–993.

[31] Kumar, A., Agarwala, V. and Singh, D. (2013). Effect of Particle Size $BaFe_{12}O_{19}$ on the microwave absorption characteristics in X-band. *Progress in Electromagnetics Research M*, 29: 223–236.

[32] Zhang, X.F., Guan, P.F. and Dong, X.L. (2010). Multidielectric polarizations in the core/shell Co/graphite nanoparticles. *Applied Physics Letters*, 96: 223111–223113.

[33] Borah, K. and Bhattacharyya, N. S. (2010). Magneto-dielectric material with nano ferrite inclusion for microstrip antennas: dielectric characterization. *IEEE Transactions on Dielectrics and Electrical Insulation*, 17: 1676 – 1681.

[34] Shin J. Y. and Oh, J. H. (1993). The microwave absorbing phenomena of ferrite microwave absorbers. *IEEE Transactions on Magnetics*, 29: 3437-3439.

[35] Feng Y. B., Qiu T. and Shen, C. Y. (2007). Absorbing properties and structural design of microwave absorbers based on carbonyl iron and barium ferrite. *Journal of Magnetism and Magnetic Materials*, 318: 8–13.

[36] Pullar R. C. (2012). Hexagonal ferrites: A review of the synthesis, properties and applications of hexaferrite ceramics. *Progress in Material Science*, 57: 1191–1334.

[37] Sjöberg, D. (2008). Analysis of wave propagation in stratified structures using circuit analogues, with application to electromagnetic absorbers. *European Journal of Physics*, 29: 721–734.

[38] Lederer, P. G. An Introduction To Radar Absorbent Materials (RAM), Report No. 85016, Royal Signals And Radar Establishment, Malvern, 1986.

[39] Oikonomou, A., Giannakopoulou, T. and Litsardakis, G. (2007). Design, fabrication and characterization of hexagonal ferrite multi-layer microwave absorber. *Journal of Magnetism and Magnetic Materials*, 316: e827–e830.

[40] Paul, J., Christopoulos, C. and Thomas, D. W. P. (1999). Generalized Material Models in TLM—Part 2: Materials with Anisotropic Properties. *IEEE Transactions on Antennas and Propagation*, 47: 1535–1542.

[41] Pozar, D. M. *Microwave Engineering*. John Wiley & Sons, USA, 4th edition, 2013.

[42] Jarvis, J. B. Transmission/reflection and short-circuit line permittivity measurements, NIST Project, Boulder, CO, Tech. Note 1341, 1990.

[43] Koledintseva M. Y., Razmadze, A. G., Gafarov, A. Y., Khilkevich, V. V., Drewniak, J. L. and Tsutaoka, T. (2011). Attenuation in extended structures coated with thin magneto-dielectric absorber layer. *Progress in Electromagnetic Research*, 118: 441–459.

[44] Chen N., Mu, G., Pan, X., Gan K. and Gu, M. (2007). Microwave absorption properties of $SrFe_{12}O_{19}/ZnFe_2O_4$ composite powders. *Material Science Engineering B*, 139: 256–260.

[45] Vinayasree S., Soloman, M. A., Sunny, V., Mohanan, P., Kurian, P. and Anantharaman, M. R. (2013). A microwave absorber based on strontium

ferrite–carbon black–nitrile rubber for S and X-band applications. *Composites Science Technology*, 82: 69–75.